Drying in nanoporous media with Kelvin effect: Capillary imbibition against evaporation by smoothed particle hydrodynamics method

Nathan Amrofel, Magdalena Dymitrowska, Amaël Obliger, Anne-Julie Tinet, Fabrice Golfier

Drying in nanoporous media with Kelvin effect: capillary imbibition against evaporation by smoothed particle hydrodynamics method.

Nathan Amrofel[1, *], Magdalena Dymitrowska[2], Amaël Obliger[3], Anne-Julie Tinet[1] and Fabrice Golfier[1]

[1] Université de Lorraine, CNRS, GeoRessources, F-54000 Nancy, France
[2] PSE-ENV/SPDR/LETIS, Institut de Radioprotection et de Sûreté Nucléaire (IRSN), Fontenay-aux-Roses, France
[3] Institut des Sciences Moléculaires, Université de Bordeaux – Bordeaux INP – CNRS, UMR 5255, F-33400 Talence, France
* Corresponding author: Bâtiment E - 2 rue du Doyen Marcel Roubault - 54505 Vandoeuvre-lès-Nancy CEDEX - France • 0.(033)7.50.90.42.72 • nathan.amrofel@univ-lorraine.fr

Understanding drying processes in nanoporous media is of great importance in many technological and industrial situations. To better understand how gas moves through clayey rocks, of interest for underground disposal of radioactive wastes, we propose using pore-scale direct numerical simulations. In this study, we use the Smoothed Particle Hydrodynamics method, which has proved to be an effective approach for simulating complex fluid dynamics within porous media at the nanoscale. Our simulations consider capillary-dominated two-phase flow with evaporation and condensation at liquid-gas interfaces, coupled to the diffusion of water vapor in the gas phase, as well as the Kelvin effect, which is a specific feature of nanopores. Our evaporation-condensation model is validated against analytical solutions. The size of the compact support of kernel function and the particle density required to obtain accurate and stable results of capillary pressure are investigated. Drying regimes, capillary-driven and evaporated-driven, are explored. A specific effort is made to highlight the influence of the Kelvin effect on desaturation and the creation of preferential paths for gas flow, as well as its impact on drying rate. The role of condensation due to local vapor concentration conditions is also emphasized.

Keywords: Liquid dynamics - Nanoporous media – Kelvin effect – Evaporation – Condensation

1. Introduction

Deep geological radioactive waste disposal projects usually foresee the burial of large quantities of metallic materials used for waste packaging and support elements, or incorporated as waste itself.

After closure of a repository, a significant amount of hydrogen is expected to be produced by both anaerobic corrosion and water hydrolysis [38]. In the case of the French Cigéo project, it is estimated that gas production will exceed the diffusion capabilities of the Callovo-Oxfordian (COx) host rock and that a distinct gas phase will appear [3,14]. For the long-term safety assessment of a repository, it is essential to thoroughly investigate how gas generation, accumulation and migration can affect its predefined properties. In particular, heat and mass transfer between the gas phase and the water-saturated pores of the host rock are expected, leading to progressive desaturation of some pores. Mass transfer of water from the liquid to the gas phase can facilitate gas phase propagation into the clay matrix and lead to formation of new percolating pathways that would otherwise be unavailable due to insufficient gas pressure as compared to the gas entry pressure [32]. On the opposite, pore resaturation may also occur locally through condensation, driven by changes in relative humidity or temperature differences between the gas phase and the rock surface, which would contribute to stabilizing the advancement of the drying front.

Mass transfer phenomena between phases are controlled by thermodynamic conditions at the liquid-vapor interfaces within the pores, and these evaporation-condensation processes have been largely studied in the context of porous media drying [2,24,32,40,45]. Direct numerical simulation methods are still being developed and improved to simulate the process of evaporation, such as the volume-of-fluid method[11,41,43], molecular dynamics[6,23,55], the level set method[31,37] and Smoothed Particle Hydrodynamics (SPH)[50,53]. However, the competition between drying forces (driven by vapor-liquid equilibrium conditions and thus by the equality of chemical potentials) and capillary forces (i.e., surface tension) becomes exacerbated as pore size decreases. Evaporation is also closely linked to diffusion, which usually prevails for low-permeability materials, since diffusion defines the ability of the gas phase to transport water vapor molecules away from the fluid interface and hence may limit the evaporation rate. As a consequence, the prediction of drying patterns in nanoporous materials remains particularly challenging and not fully understood [2,32]. The equilibrium vapor concentration, and therefore the capacity of the gas phase to accommodate water molecules in the vicinity of the water-gas interface, is generally defined through the Kelvin-Laplace equation [4]. This

relationship links thermodynamic conditions and capillary phenomena. In other words, the ability of the gas phase to contain water molecules at a given scale is depends on temperature and the local pressure difference between phases [15]. Also, some extensions of the Kelvin equation have been developed, taking into account multicomponent fluids and real gas effects [51]. For pores smaller than 8nm diameter, it is accepted that fluid properties vary across the pore, which strongly influences the validity of the Kelvin equation [4,56]. However, Boţan et al. [8] have recently demonstrated using molecular dynamics simulation the relevance of the continuous medium hypothesis for pore diameter greater than 3nm within a clayey material when slip conditions are used. This finding was supported experimentally by Yang *et al.* [52], who have shown that the Kelvin equation remains valid at a scale comparable to the size of water molecules in strongly hydrophilic capillaries.

Up to now, many studies have investigated fluid behavior and vapor transport in nanopores. Various and complex evaporation models have been developed where interfacial tension, disjoining pressure, rarefaction effect, and real gas effect [20] are taken into consideration under thermodynamic equilibrium or non-equilibrium conditions [28,30,47] but Kelvin effect has still been neglected. In contrast, other researchers [33,51] have focused on the capillary condensation phenomenon driven by the Kelvin effect. Nanopore deformation induced by condensation has been also revealed by Günther et al. [22]. Their works have provided insights into the influence of nanopore geometry on gas dynamics coupled with liquid-vapor mass transfer. However, all of these studies remain limited to a single nanopore and cannot capture the dynamics of evaporation fronts at the pore network scale. The main purpose of this study is to address this limitation.

The COx claystone presents a large pore size distribution centered between 1-100 nm, and the mesopores, i.e., between 2 and 50 nm [3] are likely to dominate its flow and transport properties. Thus, they remain within the range of validity of the Kelvin-Laplace equation. Modeling the evaporation process independently aims to study its role in easing gases migration into the clay rock in spite of important capillary pressure. Several approaches can be used for extensive pore-scale modeling. For the smallest pore sizes, molecular dynamics is preferred when validity the validity of continuum approaches is questionable, but is limited to single or double nanopores [54] due to

58 excessive computational costs. On the other side, pore network models (PNM) are largely used to
59 simulate drying patterns in larger mesoporous systems, but this phenomenological approach suffers
60 from limitations due to physical or geometrical simplifications when it comes to the understanding of
61 the drying mechanism [27,32]. A recent PNM study including Knudsen and Kelvin effects [32] has,
62 however, highlighted drastic impact of the latter phenomenon on drying patterns. In our work, the SPH
63 method has been used because of its ability to deal with interface problems while preserving a fine
64 description of physical processes [29,34,36]. An in-house SPH code has been recently developed at
65 IRSN, capable of simulating two-phase flow in a 3D porous medium sample [17,18,39]. A drying
66 algorithm with Kelvin effect, vapor diffusion, and water evaporation-condensation has been
67 implemented for the purpose of this study. The objective is to examine the contribution of various
68 mechanisms at stake and the role of coupling between these processes into the drying pattern
69 dynamics. To our knowledge, such study has never been conducted at the pore scale.

70 The structure of the article is as follows. The physical phenomena that our model takes into
71 consideration are presented in Section 2. Section 3 provides numerical discretization of the model
72 equations. In Section 4, after preliminary validation tests, we investigate the impact of the Kelvin effect
73 impact on 2D pore networks through simulations and present a sensitivity analysis of model
74 parameters. Finally, in Section 5 we resume our conclusions and discuss some perspectives for
75 application of our work within radioactive waste geological disposal projects.

76 2. Conceptual model

77 We consider hereafter a rigid porous medium whose solid skeleton constitutes *s*-phase, such as the
78 one sketched in Figure 1. The pore space is composed of mesopores, large enough so that a
79 continuum approach can be applied everywhere. The medium is initially fully saturated with liquid
80 (wetting phase, denoted by subscript *w*) in contact with gas (non-wetting phase, denoted by subscript
81 *g*). Figure 1 illustrates the overall phenomena at the scale of an idealized 2D pore network and with
82 a focus on an isolated pore. The phenomena considered at the pore scale in the present model are

vapor diffusion in the gas phase, the capillary effects (contact angle, surface curvature and tension resulting in pressure difference), evaporation and condensation including Kelvin effect,

Due to low permeability of the COx host rock, we consider the assumption of slow drying so that we have low Reynolds and Péclet numbers during our simulations. Given small characteristic length scale of the computational domain (less than a micrometer), gravity effect, density and temperature gradients are neglected. Fluid-solid interactions and the resulting disjoining pressure are also not taken into account [26]. Temperature is assumed to be constant in the system.

Water is present in gaseous (vapor) and liquid phases, and mass transfer process at gas/water interfaces is controlled by Kelvin-Laplace equation. Gas phase is considered to be composed of two components: water vapor and hydrogen. In nano- and micropores, water vapor partial pressure is much too low to maintain mechanical equilibrium at liquid-gas interface. Therefore, the total pressure in the gas phase will be treated as constant, irrespective of variations in vapor concentration. In addition, low solubility of hydrogen allows us to neglect its dissolution and diffusion in liquid phase. Finally, owing to strong adsorptive surface forces present in the COx rock, it is expected that thin water films subsist at the surface of clay minerals even after drainage [21]. While not directly considered in our model, slippage characteristic length at the gas/fluid interface should be relatively small, and thus we will neglect rarefaction effects. According to [32], the Knudsen effect does not have either a significant influence on the resulting gas invasion pattern which supports this assumption. In any case, considering Knudsen diffusion would lead to reduce the diffusion coefficient. Such parameter variation effect on the evaporation rate and the drying pattern can be analyzed through the modification of the governing dimensionless numbers as discussed hereafter (see Section 5)

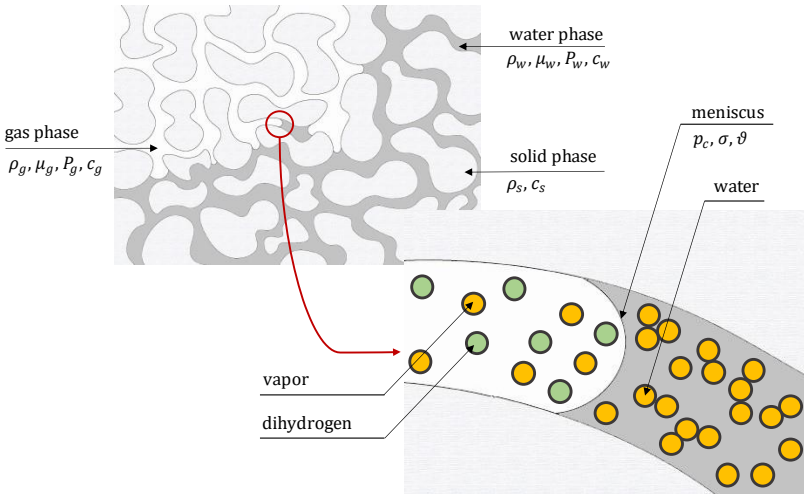

Figure 1: Schematic description of the nano-porous system as considered in this work. Gas phase progresses into clay matrix due to evaporation and diffusion of pore liquid in the form of vapor from liquid/gas interfaces.

In the following sections, the physical model and the associated equations will be detailed. We will start by presenting how the flows are modeled, taking into account transfer processes. Then, we will focus on the boundary and interface conditions.

2.1. Pore-scale equations

Description of motion of fluids as continuous phases is useful to establish force equilibrium at liquid/gas interface. At pore scale, Navier-Stokes equations in their simplified forms [42] are used to model two-phase flow of weakly compressible fluids at low Reynolds numbers. There is no external pressure acting as a driving force for fluid motion. However, particle displacements still occur, induced by capillary forces either locally from the deformation of the liquid-gas meniscus, or at the scale of the pore network where a pressure gradient may be generated by difference in capillary pressures between pore throats of different diameters. Note that all mass balance equations will be expressed

in Lagrangian formulation with the material derivative denoted D/Dt. The mass conservation for fluid phases is then stated as:

$$\frac{D\rho_{w,g}}{Dt} = -\rho_{w,g}\nabla.\boldsymbol{v}_{w,g} \quad (1)$$

with ρ density and v velocity of fluid. Indices w or g indicate the phase described (w liquid, g gas). For Newtonian fluids, the momentum equations can be expressed as:

$$\rho_{w,g}\frac{D\boldsymbol{v}_{w,g}}{Dt} = -\nabla p_{w,g} + \mu_{w,g}\Delta\boldsymbol{v}_{w,g} \quad (2)$$

with μ the dynamic viscosity of fluid and p local pressure of the fluid. Equation (2) can be also presented in its dimensionless form as:

$$Re_{w,g}\frac{D\boldsymbol{v}'_{w,g}}{Dt'} = -\frac{1}{Ca_{w,g}}\nabla p'_{w,g} + \Delta\boldsymbol{v}'_{w,g} \quad (3)$$

with $Re_{w,g} = \rho_{w,g}v_{int}L/\mu_{w,g}$, $Ca_{w,g} = \mu_{w,g}v_{int}/\sigma_{wg}$, L is the characteristic length (i.e., pore-throat size), v_{int} is an average drying velocity and σ_{wg} is the surface tension coefficient between gas and water phases. We used the following variables: $x' = x/L$, $t' = t\,v_{int}/L$, $\boldsymbol{v}'_{w,g} = v_{w,g}/v_{int}$ and $p' = p_{w,g}\,L/\sigma_{wg}$. Similar definitions hold for momentum equation in gas phase, but we will only use Re_w and Ca_w in our analysis since we will keep the density and viscosity ratio (or mobility defined as $M = \mu_w/\mu_g$) equal to one in our simulations. Such an assumption allows for a more efficient computation using SPH and remains acceptable as gravitational and viscous effects (low capillary number) are negligible compared to other phenomena in the present study. The interface displacement velocity v_{int} being expected to be very low, Reynolds number will be low enough to neglect inertial terms. In addition, the continuity of the viscous stress tensor will be ensured at fluid-fluid interfaces. The pressure p will be linked to density ρ using a linear compressibility relation :

$$p_{w,g} = c^2_{w,g}(\rho_{w,g} - \rho^0_{w,g}) \quad (4)$$

with c speed of sound, often used as a numerical parameter [12,13], and ρ^0 some reference fluid density.

The vapor can be considered as a tracer component, and we will solve mass transport by using a simple advection-diffusion equation. The most important physical parameter is then the saturated vapor concentration C_s, which is the maximum vapor concentration possible in the system at a given temperature. To model the diffusion of vapor in gas phase, Fick equation is used [7,16] as follows:

$$\frac{DC}{Dt} = \nabla.(D_v \nabla C) \quad (5)$$

with C vapor concentration in gas phase and D_v vapor diffusion coefficient. The dimensionless form of equation (5) is:

$$\frac{DC'}{Dt'} = \nabla.(\frac{1}{Pe} \nabla C') \quad (6)$$

where Péclet number is defined by $Pe = v_{int} L/D_v$ and dimensionless vapor concentration C' is equivalent to relative humidity such as $C' = C/C_s$.

Finally, to further interpret and identify the drying patterns, a dimensionless evaporation-capillary number ε will also be introduced. It is calculated as ratio between characteristic times of evaporation and capillarity. Inspired by [5,25,46], the formulation was modified to take into account pore-scale features and Kelvin effect. It can be written as follows:

$$\varepsilon = 12 \frac{Ca_w}{Pe} \Delta C' \, C_s' \quad (7)$$

with $\Delta C' = \frac{C_{eq} - C_{in}}{C_s}$ and $C_s' = \frac{C_s}{\rho_w}$. A construction of ε can be found in Appendix A.2.

2.2. Boundary conditions

Given mostly nanometric pore size distribution of COx and our model assumptions, we will use Kelvin equation (8) to locally define equilibrium vapor concentration at each liquid-gas interface. It defines

the change in ability of gas phase to accommodate water molecules, making a link between thermodynamic conditions and capillary phenomena:

$$\frac{C_{eq}}{C_s} = \exp\left(-\frac{P_c M}{\rho_w RT}\right) \quad (8)$$

where C_{eq} is equilibrium vapor concentration induced by capillary forces at curved meniscus, C_s is saturated vapor concentration, P_c capillary pressure, M is molecular weight of vapor, ρ_w density of liquid water, R universal gas constant, and T temperature. As stated before, we consider liquid phase to be saturated with all other components of the gas phase so that gases dissolution and diffusion in water can be neglected.

The difference in intermolecular interactions and/or density between two immiscible fluids causes surface tension effects at the interface between them. The resulting macroscopic force acting on particles near this interface tends to minimize its surface, and in presence of a solid surface with a wettability difference, it generates a pressure jump P_c between the two fluids. In presence of a solid phase forming a capillary tube, the law describing capillary pressure is classically written as [19]:

$$P_c = p_g - p_w = \sigma_{wg} \nabla \cdot \hat{\boldsymbol{n}} \quad (9)$$

where surface tension σ_{wg} is considered constant along the interface with $\hat{\boldsymbol{n}}$ unit vector normal to the interface. The description of interfaces between two immiscible fluids is a critical point of multiphase flow modeling by continuous methods. Capillary pressures generated at the scale of nanoscopic pores are significant (up to several tens of MPa). Under such conditions, a redistribution of pore water from larger to smaller pores occurs. Finally, at the fluid/solid interface a no-slip condition is imposed:

$$\boldsymbol{v}_{w,g}(\boldsymbol{r}_i) = 0 \quad (10)$$

where $\boldsymbol{v}_{w,g}$ denotes velocity of the fluid. Zero flux conditions are therefore applied to the walls, and mass is perfectly conserved in the system. No vapor mass transfer is supposed between gas and solid phases, and we have:

$$D_v \nabla C \cdot \boldsymbol{n}_s = 0 \quad (11)$$

where $\boldsymbol{n}_s$ is normal unit vector orthogonal to interface and pointing toward solid wall. Dirichlet condition will be applied to one external surface of porous medium:

$$C = \gamma \quad (12)$$

where γ is a constant. This condition will simulate contact with controlled-humidity air, while a no-flux condition will be imposed on the opposite side. The boundary conditions presented above, for each phase and for each phenomenon considered, will be applied in all simulations presented in this article.

3. Numerical model

In this section, a brief introduction to basic principles of SPH method will be provided, and the set of equations for evaporation-condensation model that has been presented above will be discretized. The flow equations and the curvature model have been previously presented in detail [39] and will be only briefly recalled.

3.1. SPH method

Among the methods for simulating the hydro-mechanical behavior of continuous media, the SPH is characterized by the absence of fixed mesh, its Lagrangian nature, and its remarkable adaptability to massive parallelization due to its quasi-local structure. Indeed, the medium is discretized by a cloud of material points of constant mass, and for each equation of movement is solved. In the case of fluids, these material points are often referred to as particles.

The starting point of SPH method is a convolution of a function $f(\boldsymbol{x})$ by Dirac delta function δ as follows:

$$f(\boldsymbol{x}) = \int_{\Omega} f(\boldsymbol{x}')\delta(\boldsymbol{x} - \boldsymbol{x}')d\boldsymbol{x}' \quad (13)$$

where $\boldsymbol{x}$ and $\boldsymbol{x}'$ denote positions. The properties of the Dirac delta function being $\delta(x=0)=+\infty$, $\delta(x\neq 0)=0$ and $\int_{-\infty}^{+\infty}\delta(\boldsymbol{x})d\boldsymbol{x}=1$. To create a numerically useful approximation of $f(\boldsymbol{x})$ denoted $\langle\_\rangle$, the singular form of δ is replaced by a smoothing kernel function $W(\boldsymbol{x}-\boldsymbol{x}',h)$ such as:

$$\langle f(\boldsymbol{x})\rangle=\int_{\Omega}f(\boldsymbol{x}')W(\boldsymbol{x}-\boldsymbol{x}',h)d\boldsymbol{x}'+O(h^2) \quad (14)$$

with h the smoothing length, and such that:

$$W(\boldsymbol{x}-\boldsymbol{x}',h)=0 \quad (15)$$

for $(\boldsymbol{x}-\boldsymbol{x}')\geq h$.

To ensure the consistency of the method, the kernel function $W(\boldsymbol{x}-\boldsymbol{x}',h)$ must also fulfill the following conditions:

$$\begin{cases}\lim\limits_{h\to 0}W(\boldsymbol{x}-\boldsymbol{x}',h)=\delta(\boldsymbol{x}-\boldsymbol{x}')\\ \int_{\Omega}W(\boldsymbol{x}-\boldsymbol{x}',h)d\boldsymbol{x}'=1\end{cases} \quad (16)$$

Finally, discrete approximation $\ll\_\gg$ of equations (14) is constructed by replacing the continuous form by a sum over a set of material points such that:

$$\ll f(\boldsymbol{x}_a)\gg=\sum_{b=1}^{N}\frac{m_b}{\rho_b}f(\boldsymbol{x}_b)W(\boldsymbol{x}_a-\boldsymbol{x}_b,h) \quad (17)$$

$$\ll\nabla f(\boldsymbol{x}_a)\gg=\sum_{b=1}^{N}\frac{m_b}{\rho_b}f(\boldsymbol{x}_b)\nabla W(\boldsymbol{x}_a-\boldsymbol{x}_b,h) \quad (18)$$

$$\ll\nabla.f(\boldsymbol{x}_a)\gg=-\sum_{b=1}^{N}\frac{m_b}{\rho_b}f(\boldsymbol{x}_b).\nabla W(\boldsymbol{x}_a-\boldsymbol{x}_b,h) \quad (19)$$

with $V_b=m_b/\rho_b$ the volume associated with the material point b, m_b its mass, and ρ_b its density.

The cubic B-spline function proposed by Monaghan et al. [35] has been used as kernel W:

219
$$W(\boldsymbol{x}_a - \boldsymbol{x}_b, h) = \xi \begin{cases} \frac{2}{3} - r^2 + \frac{1}{2}r^3 & 0 \le r < 1 \\ \frac{(2-r)^3}{6} & 0 \le r < 2 \\ 0 & r \ge 2 \end{cases} \quad (20)$$

220 where r is the normalized spacing between particles given by $\|\boldsymbol{x}_a - \boldsymbol{x}_b\|/h$, and ξ is a parameter
221 depending on whether the domain is defined in one, two, or three dimensions (respectively $1/h$,
222 $15/(7\pi h^2)$, and $3/(2\pi h^3)$).

223 3.2. Flow equations

224 SPH version of the continuity equation can be written as:

225
$$\frac{D\rho_a}{Dt} = \rho_a \sum_b \frac{m_b}{\rho_b} (\boldsymbol{v}_a - \boldsymbol{v}_b).\nabla W(\boldsymbol{x}_a - \boldsymbol{x}_b, h) \quad (21)$$

226 It is common to replace it by a simpler formulation, the SPH discretization equation (1) of the density
227 field, which guarantees an exact conservation of the mass:

228
$$\rho_a = \sum_b m_b W(\boldsymbol{x}_a - \boldsymbol{x}_b, h) \quad (22)$$

229 The momentum conservation equation can be written as follows:

230
$$\frac{D\boldsymbol{v}_a}{Dt} = -\sum_b \left(\frac{p_b}{\rho_b^2} + \frac{p_a}{\rho_a^2}\right) m_b \nabla W(\boldsymbol{x}_a - \boldsymbol{x}_b, h) + \sum_b \frac{4\mu_a\mu_b}{\mu_a+\mu_b} \frac{m_b}{\rho_b\rho_a} \frac{\boldsymbol{v}_a - \boldsymbol{v}_b}{\|\boldsymbol{x}_a - \boldsymbol{x}_b\|} \frac{\partial W(r_{ab}, h)}{\partial r_{ab}} + \frac{\boldsymbol{F}_s}{\rho_a} \quad (23)$$

231 Combined with a method to determine forces at the interfaces, presented hereafter, the Navier-Stokes
232 equation solved in both phases allows the establishment of a smooth fluid-fluid interface.

233 3.3. Curvature

234 We use the continuum surface force (CSF) model initially developed by Brackbill et al. [10] and widely
235 adapted and used in the SPH framework [48]. It assigns a constant color value to each particle in a
236 given phase (liquid, gas, solid). The most straightforward approach is to assign to liquid and gas SPH

particles color parameters $c_w = -1$ and $c_g = 1$, respectively. Then constant color value assigned to the solid phase is:

$$c_s(\boldsymbol{x}) = cos(\vartheta) \quad (24)$$

with ϑ contact angle between liquid and solid phases. Then it is possible to calculate $\hat{\boldsymbol{n}}$, the unit vector normal to the interface:

$$\hat{\boldsymbol{n}} = \frac{\boldsymbol{\nabla} c(\boldsymbol{x})}{\|\boldsymbol{\nabla} c(\boldsymbol{x})\|} \quad (25)$$

The local curvature of the interface κ can be calculated as:

$$\kappa = -\nabla \cdot \hat{\boldsymbol{n}} \quad (26)$$

To generate curvature at the liquid-gas interface, a volumetric surface tension force $\boldsymbol{F}_{ts}(\boldsymbol{r})$ is computed, the magnitude of which is proportional to the local curvature of the interface κ:

$$\boldsymbol{F}_{ts}(\boldsymbol{x}) = \tfrac{1}{2}\sigma_{wg}\kappa\boldsymbol{n} \quad (27)$$

For improved precision, special treatment following [1,44] is added to the color fields and to forces applied at the triple contact line (2D) to obtain equilibrium contact angle ϑ.

Within the SPH method, the color field is obtained as follows:

$$c(\boldsymbol{x}_a) = \sum_{b=1}^{N} \frac{m_b}{\rho_b} c_b W(\boldsymbol{x}_a - \boldsymbol{x}_b, h) \quad (28)$$

The color function gradient vector is calculated by discretizing equation (28) as:

$$\boldsymbol{n}(\boldsymbol{x}_a) = \sum_{b=1}^{N} \frac{m_b}{\rho_b} \big(c(\boldsymbol{x}_b) - c(\boldsymbol{x}_a)\big) \nabla W(\boldsymbol{x}_a - \boldsymbol{x}_b, h) \quad (29)$$

This allows us to determine the interface local curvature κ given by (26) as:

$$\kappa(\boldsymbol{x}_a) = \frac{1}{\|\boldsymbol{n}(\boldsymbol{x}_a)\|^2} \sum_{j=1}^{N} \frac{m_b}{\rho_b} (\boldsymbol{n}(\boldsymbol{x}_b)\|\boldsymbol{n}(\boldsymbol{x}_a)\| - \boldsymbol{n}(\boldsymbol{x}_a)\|\boldsymbol{n}(\boldsymbol{x}_b)\|). \nabla W(\boldsymbol{x}_a - \boldsymbol{x}_b, h) \quad (30)$$

Following the calculation of κ, the local resultant force $\boldsymbol{F}_{ts}(\boldsymbol{r})$ is calculated using equation (27). The spatial distribution of particles near interfaces is then ruled by the CSF model, taking into account the contact angle between the wetting and the solid phases.

3.4. Evaporation-condensation model

In this section, we present the general idea of the evaporation algorithm in which a conversion of liquid particles into gas ones takes place, as illustrated by Figure 2. We start with diffusive flux from Eq. (5) that can be discretized as follows:

$$\frac{DC}{Dt}(\boldsymbol{x}_a) = \sum_{b=1}^{N} \frac{m_b}{\rho_b} 2D_v \frac{(C_a - C_b)}{\|\boldsymbol{x}_a - \boldsymbol{x}_b\|} \frac{\partial W(\boldsymbol{r}_{ab}, h)}{\partial \boldsymbol{r}_{ab}} \quad (31)$$

where $\boldsymbol{r}_{ab} = \boldsymbol{x}_a - \boldsymbol{x}_b$. At each time step, vapor concentration C_{eq} (Eq. 8) driven by the interface curvature is imposed on gas particles located in the transition band near the liquid interface. The vapor mass injected at a gas particle i is calculated as $m_{inj} = (C_{eq}(x_i) - C(x_i)) * \frac{m_g}{\rho_g}$, where $C(x_i)$ is the preexisting vapor concentration at the particle i, m_g is the mass of gas particles and ρ_g is the density of gas particles. This mass gain is then deduced uniformly from mass counters associated with fluid particles present around x_i within the compact support of size h so that the total mass balance is verified. A similar algorithm holds for condensation. This local loss or gain of mass counters allows, in particular, for proper triggering of particle conversions to minimize mass balance instantaneous disequilibrium. The ability of gaseous particles to accommodate vapor is renewed by diffusion of the latter through the gas phase.

When the mass counter of a liquid particle reaches a mass loss equivalent to the mass of a liquid particle, a conversion into a gaseous particle is made and evaporation occurs. Similarly, when a counter of liquid particle reaches a mass gain equivalent to mass of liquid particle, the nearest gaseous particle is converted into liquid particle, and condensation occurs. The mass of a newly

condensed water particle is then uniformly subtracted from the mass counters of surrounding particles.

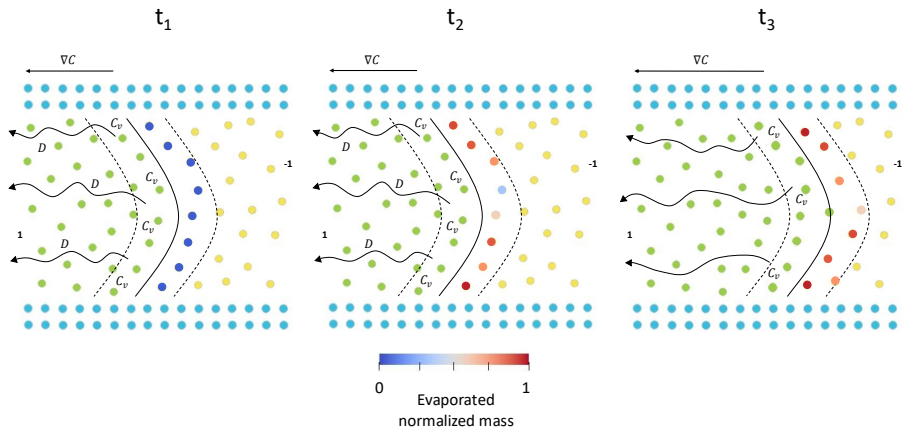

Figure 2: Illustration of SPH evaporation model. Green particles represent vapor-carrying gas, yellow particles represent water, and blue particles are solid rigid walls. The transition band is between the dashed lines. The solid line is the interface. Time t_1 is the initial time, counters are initialized to zero. The time t_2 shows the intermediary time before particle conversion. The time t_3 shows the interface moved after the conversion of some particles.

3.5. Numerical stability conditions

In the presence of viscous flow, pressure gradients, and capillary effects, minimum time step conditions must be respected to ensure stability of explicit time integration schemes. The corresponding CFL condition is detailed below:

$$\min\left\{\begin{matrix}\Delta t \le 0.125\frac{h^2}{9D}, \Delta t \le \sqrt{\frac{\frac{1}{2}(\rho_f+\rho_g)}{2\pi\sigma}h^3}, \Delta t \le 0.125\frac{\rho h^2}{\mu}, \\ \Delta t \le 0.25\frac{h}{3c}, \Delta t \le 0.25\frac{h}{\|\boldsymbol{v}_{max}\|}, \Delta t \le 0.25\frac{h}{\|\boldsymbol{a}_{max}\|}\end{matrix}\right\} \quad (32)$$

4. Validation Tests

To verify correct implementation of momentum and mass balance equations in our SPH model, we compared the numerical predictions to analytical solutions for a series of test cases and assessed the models' sensitivity to the compact support size h and the number of particles.

Each mechanism was first evaluated independently to guarantee the overall performance of the SPH model. For the sake of comparison, all results and variables will be presented dimensionless, as defined in Section 2. The different test cases with the corresponding parameter values used in the simulations are gathered in Table I. The numerical values are set so that dimensionless characteristic numbers are as close as possible to the real conditions (argillite host-rock in a disposal) while boosting calculation times and improving convergence. A sensitivity analysis of physical parameters governing evaporation and condensation processes will be performed in section 5. Some physical values will be kept constant (e.g., contact angle) for computational purposes but results will be interpreted in terms of dimensionless numbers to entangle the contribution of different mechanisms and physical parameters to the drying pattern.

Physical parameters	**Symbol**	**Value**	**Unit**
Liquid dynamic viscosity	μ_w	10^{-3}	Pa.s
Gas dynamic viscosity	μ_g	10^{-4}	Pa.s
Density ratio	ρ_w/ρ_g	1	/
Fluids sound velocities	$c_{w,g}$	5.0×10^{-1}	$m.s^{-1}$
Vapor saturation concentration	C_s	19.7	$kg.m^{-3}$
Surface tension	σ_{wg}	2×10^{-6}	$N.m^{-1}$
Contact angle	α	20	°
Characteristic length	L	1×10^{-2}	m
Diffusion coefficient	D_v	1.25×10^{-5}	$m^2.s^{-1}$

Table I: Parametrization of studied test cases.

4.1. Test case 1: Equilibrium capillary pressure between parallel plates

In order to rigorously calculate Kelvin equation at mesoscopic scale that drives evaporation, the SPH model must be capable of precisely determining the capillary pressure at liquid-gas interface in contact with solid walls. The Young-Laplace equation provides an analytical solution for simple geometries such as the 2D slit:

$$P_c = \frac{\sigma_{wg}}{R_C} = \frac{\sigma_{wg} cos(\vartheta)}{R} \quad (33)$$

with R_C radius of curvature of meniscus and R pore radius. The calculation of capillary pressure based on this equation and using mean curvature is evaluated in our SPH code.

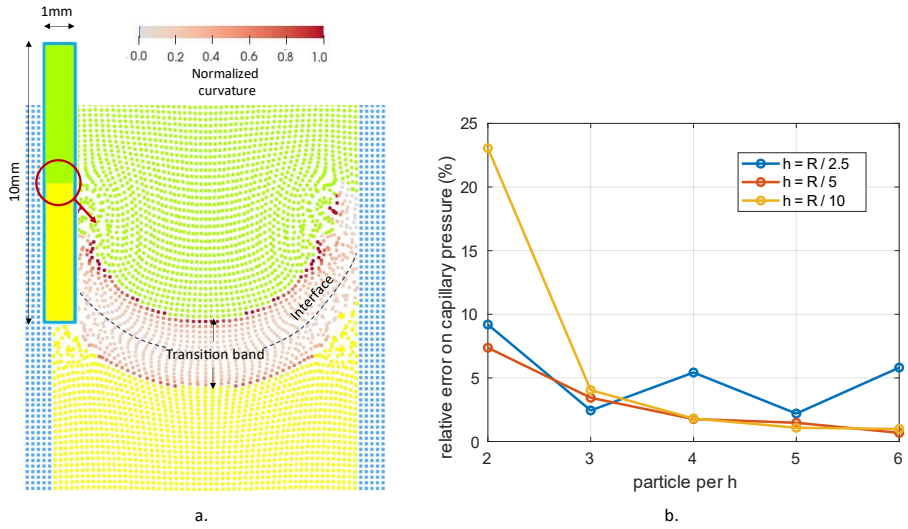

Figure 3: Verification of the SPH capillary model. a) Computational domain with a zoom on the gas-liquid interface with the solid phase in blue, the gas phase in green, and the liquid phase in yellow and red for curvature values inside the transition band. b) Relative error of numerical capillary pressure with respect to the Young-Laplace formula as a function of particle density.

We start from a closed, non-equilibrium system with two non-miscible phases (gas and water) separated by an initially flat interface. The two-dimensional simulation domain is shown in Figure 3a.

The pressure is initially the same for both fluids, and we let the system converge to mechanical equilibrium. For a given contact angle, surface tension, and constant total mass within the system, the interface between two fluids gets deformed as a result of the influence of surface tension on each phase. A pressure difference then arises at the curved interface, as predicted by the Young-Laplace equation (33). After smoothing and normalizing the curved interface using the CSF model, as detailed in Section 3.3, we infer the computed curvature radius from the 2D image, and hence the numerical value of capillary pressure from Eq. (33). A sensitivity analysis of the numerical parameters of the SPH model, namely the size of the compact support *h* and the initial particle density, is also carried out. For the sake of calculation time, the interface has the same behavior whatever the dimension studied, the capillary tube measures 1mm wide by 10mm long. The capillary number is set so that $Ca \ll 1$. The evolution with time of relative error between analytical and numerical capillary pressure values is illustrated in Fig. 3b. For sufficient high radios of compact support over pore radius (to avoid wall effects), accuracy increases with increasing number of particles. Results indicate that the precision of the computed capillary pressure vapor concentration is numerically acceptable (relative error less than 4%) for at least 5 h along the pore radius and 3 particles per h (i.e., about 28 particles per compact support of radius h). We will respect these numerical constraints in further simulations.

4.2. Test case 2: Evaporation in nanocapillary slit without capillarity and Kelvin effect

After validation of the capillary pressure evaluation for two fluids in equilibrium between flat plates, in this section the evaporation process is investigated separately. In the first step, we neglect both the Kelvin effect and capillary forces. In the absence of capillary effects, the interface between fluids is flat, and material points are not subjected to any force and therefore remain immobile. The two-dimensional simulation geometry is displayed in Figure 4. As depicted, we consider the evaporation of liquid phase through a flat and quasi-static interface coupled with the diffusion of vapor within the gas phase. The drying front behavior can therefore be considered unidimensional and can be compared with the following analytical solution (based on [7], details can be found in Appendix A.1.), which assumes a sharp transition at the interface and bulk liquid phase in which the concentration gradients are negligible:

$$d(t) = H\left(\sqrt{1 + 2\frac{D}{H^2}\frac{C_s}{\rho_w}t} - 1\right) \quad (34)$$

with $d(t) = z_1(0) - z_1(t)$ and $H = z_2 - z_1(0)$, where $z_1(t)$ is the position of the interface at time t and z_2 is the position of the boundary condition in concentration far from the liquid-gas interface. The evaporated mass and the vapor flux can be simply determined according to equation (34).

The simulation parameters are defined as follows: $C_s = 10$ kg.m^{-3} is the saturated vapor concentration, $D = 1.25 \times 10^{-5}$ m^2.s^{-1} the coefficient of vapor diffusion in gas phase and $H = 10^{-3}$m the distance between the interface $z_1(0)$ and z_2, where the vapor concentration is set to zero. The fluids are each discretized into 600 particles.

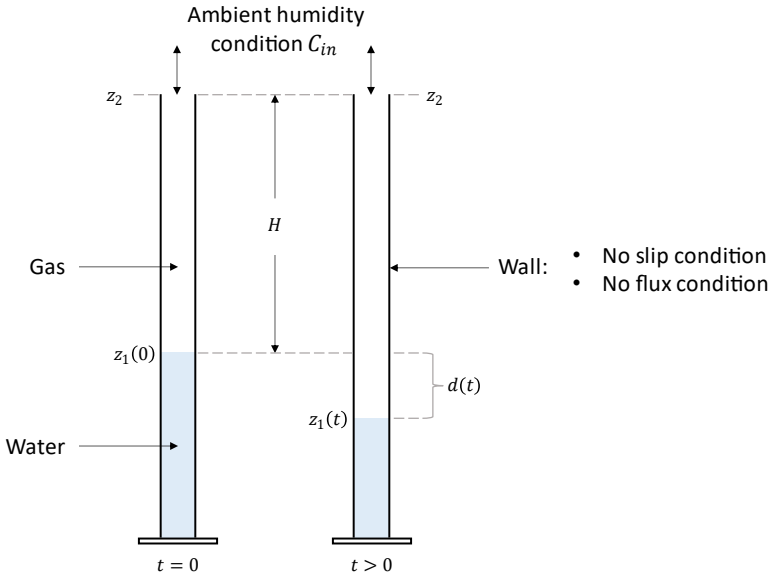

Figure 4: Geometry for simulation of evaporation between plates with quasi-stationary diffusion. The water level decreases very slowly due to evaporation and diffusion of water vapor in gas.

Figure 5 shows the relative error of the vapor mass evaporated at the interface. It is defined as the ratio between the total error of the vapor mass (i.e., the difference between the analytical and

computed vapor mass at a given time at the liquid-gas interface) and the computed value. After some initial equilibration time, the error drops to values less than 1%. The relative error on the evaporation length $d(t)$ also tends toward the error on diffused mass. The total mass conservation is automatically preserved by SPH – which is a significant asset of this method – since the particles themselves carry the mass, however, the residual error observed here comes from the choice of the evaporation algorithm and the discrete nature (mass, location) of fluid particles. Indeed, the phase conversion criterion was set at 0.5 times the mass of a water particle. Uncertainty in mass conservation is thus of the order of 0.5 of water particle mass, generating oscillations around the exact solution, as observed in Figure 5b. Another remarkable feature of the SPH method is the non-sensitivity of this technique to point organization with respect to principal axes, as illustrated in Figure 5a. The same error is found regardless of the spatial orientation of the domain, even for very small numbers of particles at the interface.

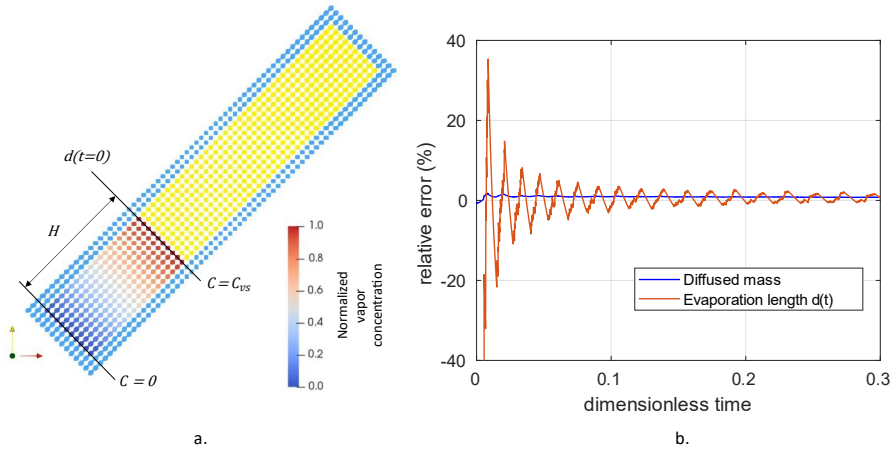

Figure 5: Verification of the SPH evaporation model without capillarity or Kelvin effect. a) simulation domain and dimensionless vapor concentration field. b) time variation of the relative error of evaporation length and vapor mass using the dimensionless time $t' = \frac{t\, v_{int}}{L_{domain}}$.

4.3. Test case 3: Evaporation in nanocapillary slit with capillary effect and Kelvin effect

This test case is similar to the previous one and based on the same numerical parameters but we take into consideration capillary and Kelvin effects as well. The analytical solution is modified by replacing the saturated vapor concentration by the equilibrium vapor concentration (7) as follows:

$$d(t) = H\left(\sqrt{1 + 2\frac{D}{H^2}\frac{C_{eq}}{\rho_w}t} - 1\right) \quad (35)$$

With parametrization chosen to reduce computational costs, the capillary pressure was too low for the Kelvin effect to be visible. Thus, the molar mass M in Eq. (8) has been artificially modified by a scaling factor of 3.25×10^8 to increase the Kelvin effect in this test case.

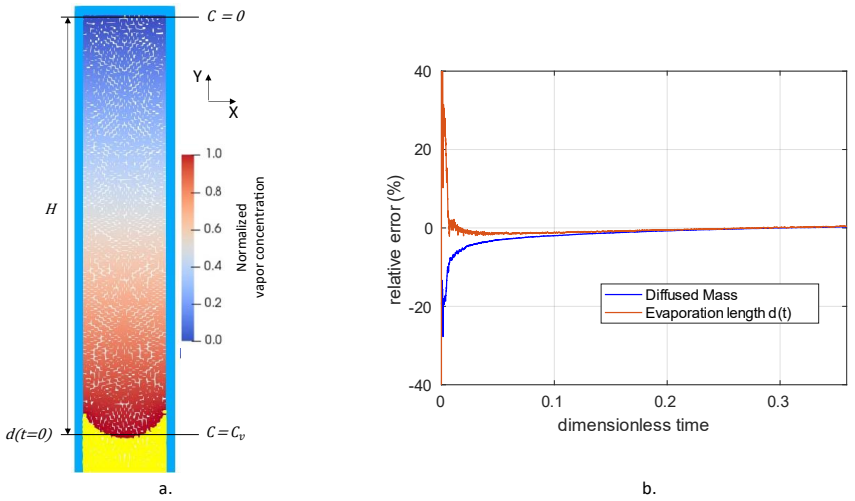

Figure 6: Verification of the SPH evaporation model with capillary and Kelvin effect. a) Geometry of the domain and dimensionless vapor concentration field. b) Relative error on the evaporation length function of dimensionless time $t' = \frac{t\, v_{int}}{L_{domain}}$.

To increase drying rate and to speed up simulations, the saturated vapor concentration is fixed at $C_s = 19.7 \times 10^{-2}$ kg.m^{-3} so that the dimensionless equilibrium vapor concentration is then $C_{eq}/C_s =$

369 0.88. For this test, 9000 fluid particles are set. The results obtained with this set of numerical
370 parameters are presented in Figure 6. The observed behavior is similar to the one observed without
371 the Kevin effect: the relative error of evaporation length tends towards the relative error of the mass
372 conservation at the interface, both are lower than 1%. As expected, the increase in number of particles
373 contributes to reducing the numerical error. In addition, the capillary forces tend to promote uniform
374 displacement of the drying front and reduce the discretization effect related to SPH since the interface
375 is smoothed between each conversion of particles.

376 ## 5. Application to nanometer-size pore networks

377 The geometry of the computational domain relies on idealized structures of connected pore networks
378 due to the complexity of imaging clayrock pore spaces with narrow pores of a few nanometers. We
379 will take advantage of this simplification to conduct a sensitivity analysis of physical parameters
380 governing evaporation and condensation processes. Note that all the dimensionless numbers
381 presented hereafter may vary locally since they are expressed at pore scale level. However, for the
382 sake of simplicity, we only consider the averaged value of these dimensionless numbers at the
383 network scale.

384 ### 5.1. Evaporation patterns and regime diagram

385 In order to observe the impact of capillary and Kelvin effects on drying patterns, we focused first on
386 2D heterogeneous arrays of narrow pores. A 3x2 pore network is used as a representative case for
387 evaporation. Interfaces labelling algorithm can be found in Appendix A.3.The channel diameters are
388 distributed between 5 and 10 nm (i.e., between $5h$ and $10h$ per radius, h being the compact support
389 length) as presented in Figure 7. Working with this type of distribution allows us to study the drying of
390 a network not accessible to gas drainage without fracturing the medium, i.e., typically for pore
391 diameters less than 20nm [9], for which the Kelvin effects are significant. The network is discretized
392 by 145000 particles, including 92000 fluid particles. For these simulations, density (ρ_w/ρ_g) and
393 viscosity (μ_w/μ_g) ratios are fixed to 1. Periodic conditions are applied to the lateral sides of the
394 domain. Gas is present at the domain top with a constant humidity condition. At the bottom boundary
395 a no-flux condition is set. A series of simulations is carried out to study the evaporation pattern's

396 dependence on capillary forces, diffusion and evaporation rates. This influence is evaluated through
397 different values of the following dimensionless numbers: *Pe*, *Ca* and the vapor density ratio $\Delta C' = \frac{C_{eq}-C_{in}}{C_s}$ (equivalent to ε), with C_{in} the vapor concentration fixed in gas phase at the top boundary. All
399 different cases with corresponding dimensionless parameter values used in the simulations are
400 gathered in Table II. For some of them, the Kelvin effect was switched off and the saturated vapor
401 concentration was used at all interfaces (cases *b.*, *e.*, *j.* and *l.*) The most representative desaturation
402 patterns are illustrated in Figure 8 (corresponding to the cases highlighted in red in Table II).

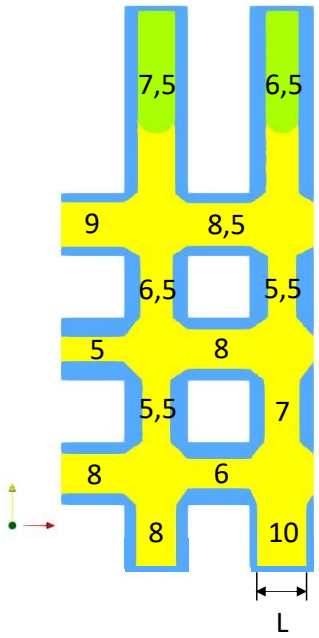

Figure 7: Initial geometry and phase distribution in the model network. The aperture is expressed in terms of compact support length h. yellow zone represents the water phase, and green ones the gas phase. Both fluid phases are surrounded by solid, rigid phase, in blue. Pores are connected laterally through periodic conditions.

403

	$\boldsymbol{\varepsilon}$	Ca_w	$\boldsymbol{Pe}$	$\Delta \boldsymbol{C'}$	$\boldsymbol{C'_{in}}$	Kelvin effect
in-situ	1.5 x 10^{-4}	5.5 x 10^{-10}	3.3 x 10^{-9}	4.0 x 10^{-1}	0.6 - 0.98	Yes
a.	1.4 x 10^{-3}	1.1 x 10^{-5}	1.7 x 10^{-4}	8.8 x 10^{-1}	0.00	Yes
b.	1.6 x 10^{-3}	1.1 x 10^{-5}	1.7 x 10^{-4}	8.8 x 10^{-1}	0.00	No
c.	1.9 x 10^{-3}	2.5 x 10^{-5}	4.1 x 10^{-4}	1.2 x 10^{-1}	0.76	Yes
d.	1.4 x 10^{-2}	1.1 x 10^{-4}	1.7 x 10^{-3}	8.8 x 10^{-1}	0.00	Yes
e.	1.6 x 10^{-2}	1.1 x 10^{-4}	1.7 x 10^{-3}	8.8 x 10^{-1}	0.00	No
f.	1.9 x 10^{-2}	2.5 x 10^{-4}	4.1 x 10^{-3}	1.2 x 10^{-1}	0.76	Yes
g.	4.5 x 10^{-2}	4.2 x 10^{-4}	6.8 x 10^{-3}	2.8 x 10^{-1}	0.70	Yes
h.	6.2 x 10^{-2}	8.2 x 10^{-4}	4.1 x 10^{-3}	1.2 x 10^{-1}	0.76	Yes
i.	1.2 x 10^{-1}	1.6 x 10^{-3}	8.2 x 10^{-3}	1.2 x 10^{-1}	0.76	Yes
j.	1.4 x 10^{-1}	1.1 x 10^{-3}	1.7 x 10^{-2}	8.8 x 10^{-1}	0.00	Yes
k.	1.6 x 10^{-1}	1.1 x 10^{-3}	1.7 x 10^{-2}	8.8 x 10^{-1}	0.00	No
l.	4.4 x 10^{-1}	3.4 x 10^{-3}	1.7 x 10^{-2}	8.8 x 10^{-1}	0.00	Yes
m.	5.0 x 10^{-1}	3.4 x 10^{-3}	1.7 x 10^{-2}	8.8 x 10^{-1}	0.00	No
n.	1.6 x 10^{0}	1.1 x 10^{-2}	1.7 x 10^{-3}	1.0 x 10^{0}	0.00	Yes

Table II: Dimensionless parametrization for studied cases sorted by increasing $\boldsymbol{\varepsilon}$. The cases colored in red correspond to patterns illustrated in Figure 9. For the sake of comparison, the expected in situ conditions for COx are also given.

A regime diagram $Ca - \varepsilon$ is illustrated in Figure 8 and confirms the role of ε in delineating the drying patterns. Note that each of the dimensionless parameters has varied by several orders of magnitude to demonstrate the unique dependency on the evaporation-capillary number at this scale (see Table II). For the sake of comparison, the ε value for the representative in situ conditions in COx formation (based on data from [3,9]) is also indicated in Table II. It is quite remarkable to observe that, in spite of drastically different values for Ca and Pe, the ε value for in situ conditions is quite similar to the range of values explored in our study (10^{-4} against 10^{-3} for the lowest value simulated numerically),

411 and hence, the expected evaporation pattern (corresponding to the capillary dominated regime) can
412 be inferred from these simple simulations. Similar reasoning holds for the impact of parameter
413 variations. For instance, reducing the contact angle will increase the capillary pressure and the
414 meniscus curvature at the interface. From Eq. (8), it will decrease the equilibrium vapor concentration
415 C_{eq} and slow down the local evaporation rate by exacerbating the Kelvin effect. As a consequence, it
416 will enhance front instability and so a transition towards capillary dominated regime (lower ε).

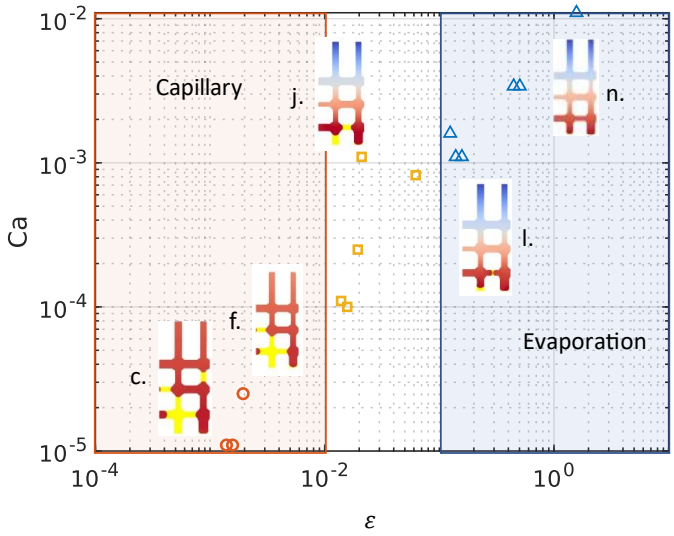

417

Figure 8: Drying regimes diagram as a function of capillary-evaporation number for evaporation simulations with capillary and/or Kelvin effects.

418 As depicted in Figure 8 and highlighted in Figure 9 with the two most extreme cases, two
419 representative regimes are revealed: the capillary-dominated regime (e.g. case *g.* with a high ambient
420 humidity condition) and the evaporation-dominated regime (e.g. case *n.*). The temporal evolution of
421 water desaturation for the two most extreme cases, representative of evaporation and capillary
422 regimes exhibits strong heterogeneity in the capillary-dominated regime while demonstrating a
423 homogeneous desaturation front for the evaporation regime. Of course, boundaries shown in Figure

424 8 have been drawn between the different regimes based on a qualitative observation of the
425 evaporation structures and some uncertainties may be associated with the transition lines.

426 The concentration field will be crucial as it will significantly accentuate the presence of heterogeneities
427 in the patterns, especially when surpassing the local vapor equilibrium conditions at the interfaces.
428 The evaporation rate is also critical as it will determine whether or not liquid redistribution occurs
429 within the network.

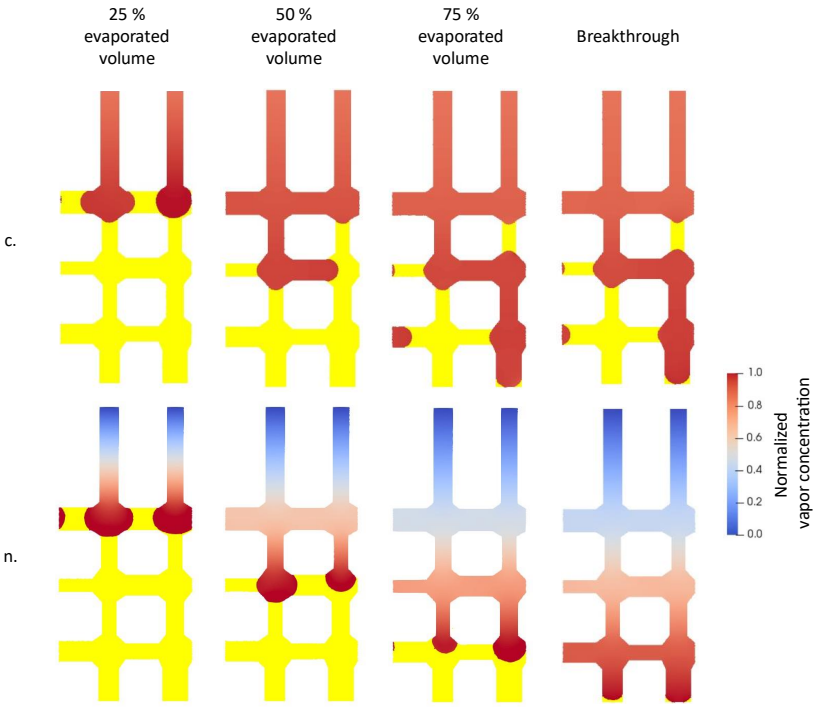

430

Figure 9: Evolution with time of vapor concentration fields and fluid distribution patterns for the test cases c) and n). The comparison is made at equivalent evaporated volumes and on a normalized vapor concentration scale. The liquid phase is represented in yellow.

431 The capillary-dominated drying regime corresponds to conditions of very low ε ($\varepsilon < 1 \times 10^{-2}$).
432 Capillary forces are high enough to prevent evaporation in the smallest pores, which remain saturated.

433 The equilibrium vapor concentration at the liquid-gas meniscus in such pores is lower than the vapor
434 concentration in the surrounding gas, and vapor cannot be diffused away from the meniscus. This
435 results in the formation of preferential evaporation pathways (Figure 9*c*). This phenomenon is
436 accentuated by the Kelvin effect. A similar situation takes place with increased inlet vapor
437 concentration and hence, reduced evaporation rate. The higher the ambient humidity conditions, the
438 fewer pores will have the ability to empty and the more heterogeneous the drying pattern will be
439 (Figure 9*c*). At the macroscale, the residual water saturation is higher (Figure 10). It may also facilitate
440 the formation of disconnected water clusters if the pore size distribution is large enough.
441 In contrast, for high values of ε ($\varepsilon > 1 \times 10^{-1}$), evaporation rate and viscous forces have taken
442 advantage over capillary forces. All the pores in contact with the gas front evaporate at the same time.
443 A uniform drying pattern is observed with practically no residual water saturation (Figure 9*n*, 10). This
444 is an evaporation-dominated regime. The impact of the Kelvin effect is negligible at low ambient
445 humidity, with the drying front being uniform (Figure 9.n).

446 Between these two values ($1 \times 10^{-2} > \varepsilon > 1 \times 10^{-1}$), the gas invasion pattern becomes transient
447 between capillary-dominated and evaporation-dominated. In this intermediate regime, both capillary
448 forces and the evaporation rate are competing. Small desaturation front inhomogeneities may appear,
449 but they do not propagate very far (Figure 8.j), as we can also see later (Figure 11).

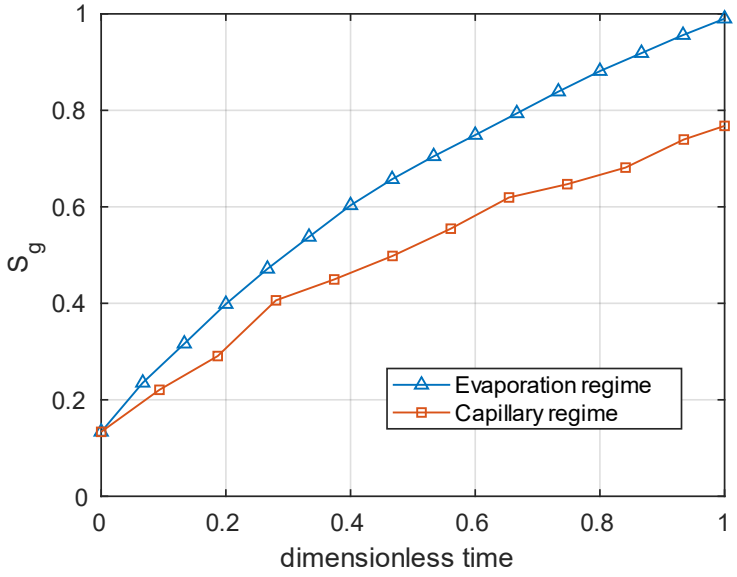

Figure 10: Evolution of gas saturation with dimensionless time for capillary-dominated (case *c.*) and evaporation-dominated (case n.) regimes.

This discrepancy between these two contrasted drying regimes is also visible in the drying dynamics. As illustrated in Figure 10, the evolution of gas saturation S_g with dimensionless time changes drastically from the evaporation to the capillary-driven regime. For the first one, gas saturations increases like a 1D analytical solution ($\sim\sqrt{Dt}$) with time and slows down only close to breakthrough time due to mass transfer limitations [7]. In contrast, in the capillary-driven regime, gas saturation at breakthrough is significantly lower (75% against 100%) due to the formation of preferential pathways for drying and the presence of residual water clusters. The heterogeneity of pore size distribution in the medium, combined with the low value of capillary number and the Kelvin effect, results in the strong variability of the equilibrium vapor concentration at different gas-liquid menisci along the drying front. It thus induces variations in drying rates with time, as shown in Figure 10.

5.2. Kelvin effect on gas invasion pattern

In addition to the previous test cases summarized in Table I, we performed supplementary simulations on one larger pore network in order to investigate further the impact of Kelvin effect and to determine to what extent it may affect gas invasion patterns and to avoid possible boundary effects. These simulations were carried out with or without Kelvin effect on a 5x5 heterogeneous network with mean pore radius of 7.78 nm and a standard deviation of 1.64 nm (corresponding to a range of pore sizes from 5 to 10 nm) under the same conditions that were presented for cases j. and k. in Section 5.1. We set the density and viscosity ratio to one, the capillary number is around 10^{-3} and the Péclet number is about 10^{-2}, with a constant vapor concentration imposed at the inlet, corresponding to $C_{in}^{'} = 0.75$. Such conditions lead to an evaporation-capillary number equal to $\varepsilon \approx 1.4 \times 10^{-1}$ and $\varepsilon \approx 1.6 \times 10^{-1}$ for the simulations with and without the Kelvin effect, respectively. Based on these values, we expect a capillary-dominated regime, more pronounced with the Kelvin effect. In addition, Kelvin effect induces a significant decrease in equilibrium vapor concentration, which varies over the range of pore sizes from $0.77C_s$ to $0.88C_s$ at different menisci.

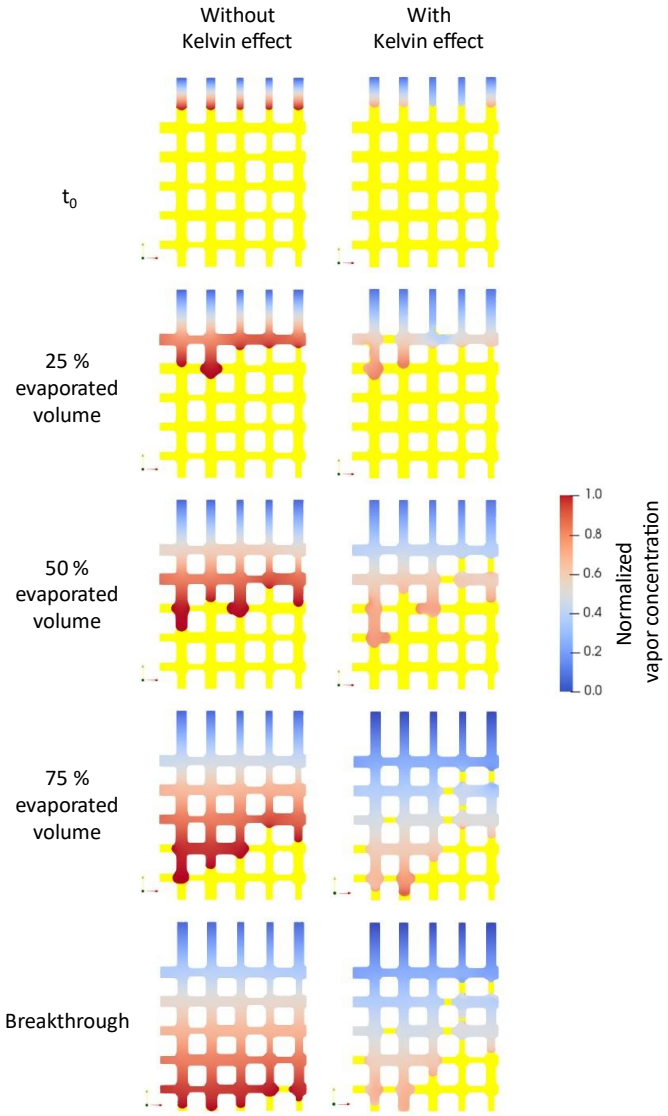

Figure 11: 5x5 network. Comparison of evaporation fronts without (left) and with Kelvin effect (right) at two different equivalent evaporated volumes and on a normalized vapor concentration scale. The water phase is represented in yellow. Periodic conditions are applied to side domain boundaries. Gas invasion is made from the top with $C_{in}^{'} = 0.75$*. The domain is closed at the bottom.*

In order to highlight the Kelvin effect's impact on drying patterns, Figure 11 compares, at equivalent gas saturation, the fluids' distributions within the pore space in the presence (right) or absence (left) of the Kelvin effect. The network is obviously less saturated with water vapor from the initial time. It generates competition between channels with variable drying front velocities from one pore to another, leading to complex fluid redistribution. As expected, front inhomogeneities appear to be more important with the Kelvin effect, but they remain limited due to the small size of the domain. From 25% evaporation, the Kelvin effect modifies the drying pattern by closing the smallest pores, due to local vapor concentration conditions. The most advanced front is located in a different pore. A pore channel that is dried slower may catch up the head of the front at a later stage (e.g., between 50% and 75% for the cases presented in Figure 11), and a quasi-uniform gas front can even be recovered when the breakthrough is occurring. This last phenomenon is largely accentuated by the absence of the Kelvin effect. In the presence of the Kelvin effect, the front is much less uniform. Between 50% and 75% evaporation, we can have up to three channels of difference in drying, or half of the network. Also, many channels remain filled with water upstream of the network. As on the smaller networks, the Kelvin effect with high ambient humidity significantly accentuates heterogeneities, with the appearance of disconnected clusters of the liquid phase (Figure 11), so that breakthrough occurs at 78.6% of gas saturation compared to 97.8% without the Kelvin effect.

Another remarkable finding, not highlighted in previous studies, is the impact of condensation on the gas invasion pattern, made possible by Kelvin effect. Due to possibility for equilibrium vapor concentration at the meniscus will become lower than the ambient vapor concentration flowing through the pore space, residual water clusters trapped behind the front may promote condensation. We have illustrated this mechanism in Figure 12 for test case h. where we have represented at different times the mass transported by liquid particles close to the interface in the transition band (a negative value implies vapor loss and so, water condensation) and the relative humidity within the gas phase (the color scale ranges between the relative humidity at equilibrium and the highest value in the gas phase). In the presence of Kelvin effect, capillary forces induced by the throat size of 5.5 nm reduce equilibrium relative humidity to 0.79. In addition, the vicinity of the drying front in the lower

part favors high ambient vapor concentrations in the gas phase (Figure 12, time t_1). This results in a displacement of vapor from higher (gas phase) to lower (gas-liquid interface) concentrations, and hence, condensation occurs (Figure 12, time t_2). The liquid cluster expands, but in the upward direction, because of capillary forces that force water to move into the narrowest pore (Figure 12, time t_3). This mechanism can be quite fast, with local condensation rates much higher than the average drying rate. The velocity $\boldsymbol{v}$ at which the interface moves to fill the pore by condensation is of the same order as the velocity $\boldsymbol{v}_{int}$ at which the drying front moves in the system such that $\boldsymbol{v}/\boldsymbol{v}_{int} \sim 1$. It could contribute to reducing the vapor concentration at the front head, and hence, increasing the vapor gradient, and speed up the evaporation breakthrough.

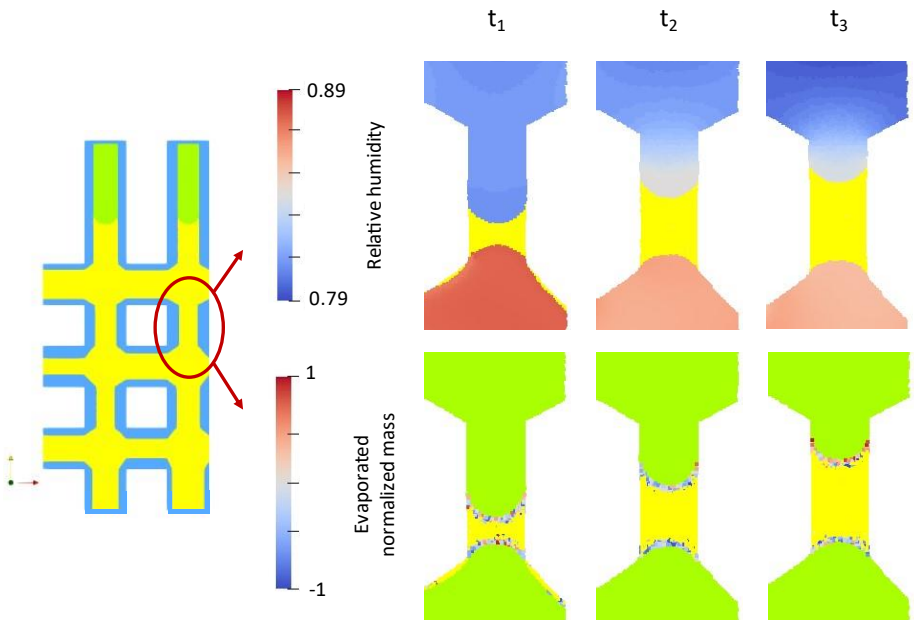

Figure 12: Evidence of the filling of the smallest pores by condensation at different times. Top: Concentration fields of dimensionless vapor concentration (relative humidity) in the gas phase. Bottom: The water phase is in yellow. The color field shows the local mass balance per liquid particle in the transition band before conversion. A positive balance leads to evaporation. A negative balance leads to condensation.

Finally, as expected, these differences in evaporation patterns also affect the dynamics of drying. The evolution of gas saturation with dimensionless time, illustrated in Figure 13, shows a similar trend for both curves but with a lower gas saturation to breakthrough in the presence of the Kelvin effect. Note that the dimensionless time is here defined for both simulations using the front velocity v_{int} without the Kelvin effect. The impact of mass transfer limitations is more pronounced than in Section 5.1 due to the larger pore network size, but no fluctuation of front velocity occurs, probably because the heterogeneity of the pore size distribution is not large enough. The drying rate is also reduced because equilibrium vapor concentrations are smaller than the saturated vapor concentrations, and in spite of preferential pathways. This is consistent with the experimental results of Thiery et al. [45]. Note that PNM simulations by Maalal *et al.* [32] predict the opposite result of the Kelvin effect on time to breakthrough, probably because the impact of pattern instabilities prevails. This competition, driven by the Kelvin effect between the reduction of local equilibrium vapor concentration and the development of preferential pathways, will require further investigation.

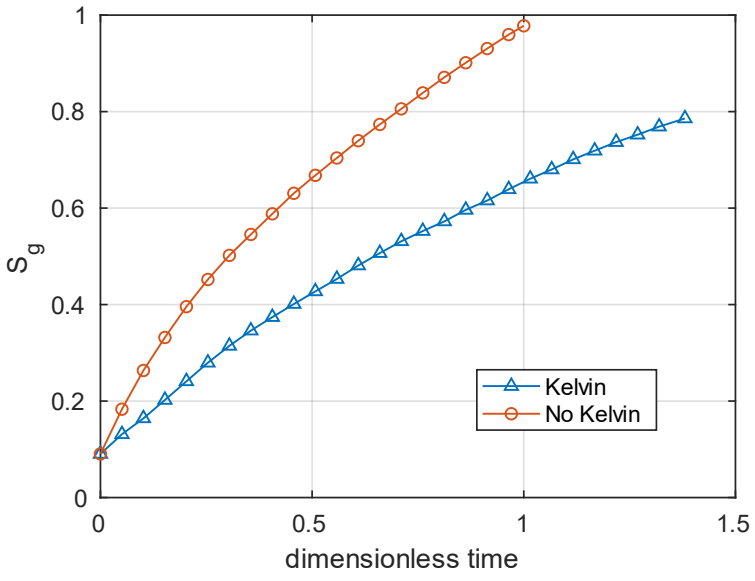

Figure 13: Evolution of gas saturation with dimensionless time with and without the Kelvin effect.

6. Conclusion

The desaturation process in nanoporous rocks can be considerably affected by liquid evaporation, especially when the smallest pores cannot be dewatered due to insufficient gas pressure to overcome capillary barriers. This mechanism is usually neglected or oversimplified in models investigating gas drainage. Consequently, in this article, we built an evaporation model to predict gas dynamics at pore scale. All key mechanisms are considered, including mass transport of vapor in gas phase, capillary forces, and the Kelvin effect. The present work also takes into account fluids and solid properties, and ambient humidity in the evaporation process.

We have used a SPH code to enhance multiphase modeling. Accurate calculation of capillary pressures at interfaces allowed us to correctly estimate liquid redistribution in the porous medium and local equilibrium vapor concentration at curved menisci according to Kelvin equation. We were able to estimate the minimum size of the compact support and particle density required to obtain stable and accurate results (relative errors of less than 1%).

We were able to demonstrate the ability of our continuous SPH model to simulate evaporation-condensation phenomena driven by Kelvin effect and vapor diffusion through gas phase. This model has been validated using analytical solutions. Drying simulations of small pore networks allowed us to highlight two desaturation regimes separated by an intermediate regime for ε parameter between 10^{-3} and 1. Kelvin effect has been shown to drastically influence both gas distribution patterns and drying dynamics within the capillary-dominated regime. A comparative analysis of our results and those from the literature revealed that Kelvin condition induces contrasted behavior with a reduction of equilibrium vapor concentration and the development of preferential gas pathways. They may affect gas dynamics in opposite ways and result in increasing or decreasing time to breakthrough. The condensation phenomenon has also been observed in the vicinity of drying front and, depending on the local vapor saturation conditions, may slow down or block gas invasion into smallest pores. In some cases, pores may even refilled with water.

As a final word, we have highlighted in this paper the importance of the Kelvin effect on the formation of gas percolation channels, particularly in high-humidity conditions. These findings align with existing literature, encompassing both numerical and experimental studies. They underscore the significance of considering nanoscopic phenomena, such as the Kelvin effect, when upscaled studies are conducted. In the future, we would like to couple evaporation to drainage flow and to consider hydro-mechanical coupling that may promote creation of dilatant pore pathways and thus gas migration [14,39]. Improving description of evaporation and capillary condensation processes into the smallest pores when the Kelvin equation fails by bridging the gap between molecular methods and continuous methods is also an avenue for future work.

Appendices

A. Analytical solution of evaporation with quasi-steady-state diffusion

In order to find the 1D analytical solution for the problem in Figure 4, we define the diffusive flux as:

$$\varphi_w = -D_v \nabla C \cdot \boldsymbol{n}_s \tag{36}$$

With $\frac{\partial C}{\partial x} = \frac{\partial C}{\partial y} = 0$ and D_v the diffusion of vapor in gas. At the water/gas interface, at $z = z_1$, equation (36) can be written as:

$$\varphi_w|_{z=z_1} = -D_v \left.\frac{\partial C}{\partial z}\right|_{z=z_1} = \frac{D_v}{z_2 - z_1(t)}\left(\rho_{eq} - \rho_{in}\right) \tag{37}$$

Considering a very slow liquid retreat, we use the quasi-steady state method:

$$-\rho_w \frac{dz_1}{dt} = \frac{D}{z_2 - z_1(t)}\left(\rho_{eq} - \rho_{in}\right) \tag{38}$$

so that we have the following equation:

$$(z_2 - z_1(t))dz_1 = \frac{D}{\rho_w}\rho_{eq}dt \quad (39)$$

We use $d(t) = z_1(0) - z_1(t)$ and $H = z_2 - z_1(0)$ to integrate equation (39) as:

$$\int_0^d (H + d)\, dd = \frac{D}{\rho_w}\rho_{eq}\int_0^t dt \quad (40)$$

Therefore :

$$\frac{1}{2}(H + d)^2 - \frac{1}{2}H^2 = \frac{D}{\rho_w}\rho_{eq}t \quad (41)$$

Finally, the analytical solution for the interface displacement is written as follows:

$$d(t) = H\left(\sqrt{1 + \frac{D}{H^2}\frac{\rho_{eq}}{\rho_w}t} - 1\right) \quad (42)$$

B. Evaporation-capillary number definition

Considering only diffusion, flux at liquid-gas interface can be written as:

$$\varphi_w = -D_v \nabla C \cdot \boldsymbol{n}_s \quad (43)$$

By using quasi-steady-state assumption, we can write from (38) the dimensionless variation of the position due to evaporation as:

$$\frac{dz_1{}'}{dt'} = -\frac{D_v}{v_0 L}\frac{C_{eq} - C_{in}}{C_s}\frac{C_s}{\rho_w}\nabla C' = -\frac{1}{Pe}\Delta C\, C_s' \nabla C' \quad (44)$$

The dimensionless Navier-Stokes equation can be written as:

$$Re\frac{D\boldsymbol{v}'}{Dt} = -\frac{1}{Ca}\nabla p' + \Delta \boldsymbol{v}' \quad (45)$$

By solving this equation with Washburn assumptions [49], we can write the dimensionless variation of the position due to capillary effects as:

$$\frac{dz_1{}'}{dt'} = -\frac{\nabla p'}{12Ca} r'^2 \qquad (46)$$

From equation (37) and (39) we can assess the characteristic time of imbibition and evaporation. By dividing the first by the second, we obtain the following equation:

$$\frac{\tau_{imbib}}{\tau_{evap}} = 12\,\frac{Ca}{Pe}\,\frac{C_{eq} - C_{in}}{C_s}\,\frac{C_s}{\rho_w}\,\frac{\partial C'}{r'\partial p'} \qquad (47)$$

Here we can recognize the dimensionless evaporation-capillary number.

C. Interface particle labelling

Evaporation in COx clayey rock is influenced by nanoscopic effects. In order to take these effects into account, the Kelvin equation has been implemented in the SPH method. To remain consistent with the assumption of the surface tension independent of the distance to the solid wall and to damp any non-physical local fluctuations, the capillary pressure is averaged over each liquid-gas interface. To be able to determine the mean capillary pressure per interface, we must be able to discriminate the particles according to the interface to which they "belong". Figure 14 presents the overall concept of the algorithm performing this task.

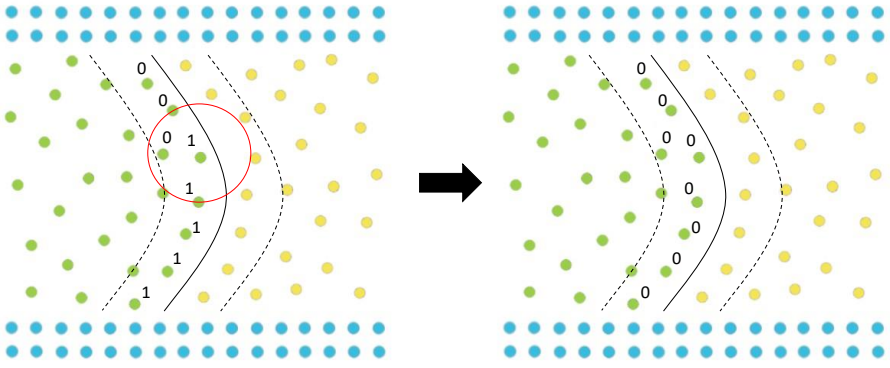

Figure 14: Labelling steps of interfaces particles when two labels are on the same compact support.

The principle is the following: we loop over all the particles belonging to a transition band, assigning them a label. During this loop, two cases can happen:

- The particle had not yet been labeled; in which case it was given a new label (N+1, N being the highest existing label).
- The particle has already been labeled (label M); nothing happens.

Each time a particle is labeled, particles on its compact support are checked:

- The particle had not yet been labeled; in which case it is given same label as the central particle (M or N+1)
- The particle has already been labeled (label K); the particle having the highest label of the two turns into the smallest label, as shown figure 14.

This algorithm leads to distinguished interfaces is they are separated by a distance bigger than h.

The characteristic time of evaporation must be greater than the characteristic time of establishment of the interface in order not to degrade the calculus of capillary pressure. If this condition is fulfilled, the capillary effects will allow smoothing of the interface.

Acknowledgments

This project has received funding from Euratom research and training programme 2014-2018 under grant agreement N°847593 (EURAD) and from NEEDS programme (MECHE).

Data Availability Statement

The data that support the findings of this study are available from the corresponding author upon reasonable request.

[1] S. Adami, X.Y. Hu, N.A. Adams, Contact line hydrodynamics with SPH, in: Prato, Italy, 2012.
[2] F. Ahmad, M. Talbi, M. Prat, E. Tsotsas, A. Kharaghani, Non-local equilibrium continuum modeling of partially saturated drying porous media: Comparison with pore network simulations, Chemical Engineering Science 228 (2020) 115957.
[3] ANDRA, Évalution phénoménologique du stockage géologique, Agence Nationale pour la gestion des Déchets Radioactifs, 2005.
[4] E. Barsotti, S.P. Tan, S. Saraji, M. Piri, J.-H. Chen, A review on capillary condensation in nanoporous media: Implications for hydrocarbon recovery from tight reservoirs, Fuel 184 (2016) 344–361.
[5] E.M. Benner, D.N. Petsev, Evaporation effect on two-dimensional wicking in porous media, Journal of Colloid and Interface Science 514 (2018) 21–29.
[6] E. Bird, J. Gutierrez Plascencia, P. Keblinski, Z. Liang, Molecular simulation of steady-state evaporation and condensation of water in air, International Journal of Heat and Mass Transfer 184 (2022) 122285.
[7] R.B. Bird, W.E. Stewart, E.N. Lightfoot, Transport phenomena, 2nd, Wiley international ed ed., J. Wiley, New York, 2002.
[8] A. Boţan, B. Rotenberg, V. Marry, P. Turq, B. Noetinger, Hydrodynamics in Clay Nanopores, J. Phys. Chem. C 115 (2011) 16109–16115.
[9] P. Boulin, Expérimentation et modélisation du transfert d'hydrogène à travers des argiles de centre de stockage de déchets radioactifs, These de doctorat, Grenoble INPG, 2008.
[10] J.U. Brackbill, D.B. Kothe, C. Zemach, A continuum method for modeling surface tension, Journal of Computational Physics 100 (1992) 335–354.
[11] L. Bureš, Y. Sato, Direct numerical simulation of evaporation and condensation with the geometric VOF method and a sharp-interface phase-change model, International Journal of Heat and Mass Transfer 173 (2021) 121233.
[12] A. Colagrossi, A meshless Lagrangian method for free surface and interface flows with fragmentation., PhD Thesis, University of Rome, 2005.
[13] A. Colagrossi, M. Landrini, Numerical simulation of interfacial flows by smoothed particle hydrodynamics, Journal of Computational Physics 191 (2003) 448–475.
[14] R. Cuss, J. Harrington, R. Giot, C. Auvray, Experimental observations of mechanical dilation at the onset of gas flow in Callovo-Oxfordian claystone, Geological Society, London, Special Publications 400 (2014) 507–519.
[15] J.-F. Daïan, Fluids in Equilibrium in the Pore Space: Capillary Behavior, in: Equilibrium and Transfer in Porous Media 1: Equilibrium States, John Wiley & Sons, Ltd, 2014: pp. 1–19.
[16] J.-F. Daïan, Equilibrium and Transfer in Porous Media 2: Transfer Laws | Wiley, Wiley.Com (2014).
[17] R.C. Deptulski, Modelling damage and dilatant two-phase flow at pore scale using Smoothed Particle Hydrodynamics (SPH) method, phdthesis, Sorbonne Université, 2021.
[18] R.C. Deptulski, M. Dymitrowska, D. Kondo, Modelling non-local elasticity in 1D vibrating rods using Corrected Smoothed Particle Hydrodynamics method, European Journal of Mechanics - A/Solids 91 (2022) 104403.
[19] R. Finn, Equilibrium Capillary Surfaces, Springer, New York, NY, 1986.
[20] J. Fu, Y. Su, Z. Chen, L. Li, W. Wang, S. Zhan, Distribution of a water film confined in inorganic nanopores in real shale gas reservoirs, Journal of Petroleum Science and Engineering 209 (2022) 109831.
[21] T. Gimmi, S.V. Churakov, Water retention and diffusion in unsaturated clays: Connecting atomistic and pore scale simulations, Applied Clay Science 175 (2019) 169–183.
[22] G. Günther, J. Prass, O. Paris, M. Schoen, Novel Insights into Nanopore Deformation Caused by Capillary Condensation, Phys. Rev. Lett. 101 (2008) 086104.
[23] Y. Guo, X. Zhao, F. Zhao, Z. Jiao, X. Zhou, G. Yu, Tailoring surface wetting states for ultrafast solar-driven water evaporation, Energy Environ. Sci. 13 (2020) 2087–2095.
[24] Z. Huang, B. Chen, X. Mo, X. Yang, L. Yu, X. Hu, K. Liu, Fast Water Evaporation from Nanopores, Advanced Materials Interfaces 8 (2021) 2100660.
[25] J. Hyväluoma, P. Raiskinmäki, A. Jäsberg, A. Koponen, M. Kataja, J. Timonen, Simulation of liquid penetration in paper, Phys. Rev. E 73 (2006) 036705.

[26] J.N. Israelachvili, ed., Intermolecular and Surface Forces, in: Intermolecular and Surface Forces (Third Edition), Academic Press, Boston, 2011: p. iii.
[27] P. Lefort, Etude des déplacements eau-gaz dans les argilites du callovo-oxfordien à l'aide de la théorie de la percolation en gradient, These de doctorat, Toulouse, INPT, 2014.
[28] R. Li, J. Wang, G. Xia, New Model for Liquid Evaporation and Vapor Transport in Nanopores Covering the Entire Knudsen Regime and Arbitrary Pore Length, Langmuir 37 (2021) 2227–2235.
[29] M.B. Liu, G.R. Liu, Smoothed Particle Hydrodynamics (SPH): an Overview and Recent Developments, Arch Computat Methods Eng 17 (2010) 25–76.
[30] Z. Lu, S. Narayanan, E.N. Wang, Modeling of Evaporation from Nanopores with Nonequilibrium and Nonlocal Effects, Langmuir 31 (2015) 9817–9824.
[31] K. Luo, C. Shao, M. Chai, J. Fan, Level set method for atomization and evaporation simulations, Progress in Energy and Combustion Science 73 (2019) 65–94.
[32] O. Maalal, M. Prat, D. Lasseux, Pore network model of drying with Kelvin effect, Physics of Fluids 33 (2021) 027103.
[33] M. Miyahara, H. Kanda, T. Yoshioka, M. Okazaki, Modeling Capillary Condensation in Cylindrical Nanopores: A Molecular Dynamics Study, Langmuir 16 (2000) 4293–4299.
[34] J.J. Monaghan, Smoothed particle hydrodynamics, Rep. Prog. Phys. 68 (2005) 1703–1759.
[35] J.J. Monaghan, J.C. Lattanzio, A refined particle method for astrophysical problems, Astronomy and Astrophysics 149 (1985) 135–143.
[36] J.P. Morris, P.J. Fox, Y. Zhu, Modeling Low Reynolds Number Incompressible Flows Using SPH, Journal of Computational Physics 136 (1997) 214–226.
[37] B.M. Ningegowda, Z. Ge, G. Lupo, L. Brandt, C. Duwig, A mass-preserving interface-correction level set/ghost fluid method for modeling of three-dimensional boiling flows, International Journal of Heat and Mass Transfer 162 (2020) 120382.
[38] L. Ortiz, G. Volckaert, D. Mallants, Gas generation and migration in Boom Clay, a potential host rock formation for nuclear waste storage, Engineering Geology 64 (2002) 287–296.
[39] A. Pazdniakou, M. Dymitrowska, Migration of Gas in Water Saturated Clays by Coupled Hydraulic-Mechanical Model, Geofluids 2018 (2018) e6873298.
[40] M. Prat, Recent advances in pore-scale models for drying of porous media, Chemical Engineering Journal 86 (2002) 153–164.
[41] J. Reutzsch, C. Kieffer-Roth, B. Weigand, A consistent method for direct numerical simulation of droplet evaporation, Journal of Computational Physics 413 (2020) 109455.
[42] J. Salençon, Modelling the Continuum, in: J. Salençon (Ed.), Handbook of Continuum Mechanics: General Concepts Thermoelasticity, Springer, Berlin, Heidelberg, 2001: pp. 1–30.
[43] N. Scapin, P. Costa, L. Brandt, A volume-of-fluid method for interface-resolved simulations of phase-changing two-fluid flows, Journal of Computational Physics 407 (2020) 109251.
[44] R. Sivanesapillai, N. Falkner, A. Hartmaier, H. Steeb, A CSF-SPH method for simulating drainage and imbibition at pore-scale resolution while tracking interfacial areas, Advances in Water Resources 95 (2016) 212–234.
[45] J. Thiery, S. Rodts, D.A. Weitz, P. Coussot, Drying regimes in homogeneous porous media from macro- to nanoscale, Phys. Rev. Fluids 2 (2017) 074201.
[46] C. Van Engeland, B. Haut, L. Spreutels, B. Sobac, Evaporation versus imbibition in a porous medium, Journal of Colloid and Interface Science 576 (2020) 280–290.
[47] J. Wang, G. Xia, R. Li, Numerical analysis of evaporation from nanopores using the direct simulation Monte Carlo method, Journal of Molecular Liquids 347 (2022) 118348.
[48] Z.-B. Wang, R. Chen, H. Wang, Q. Liao, X. Zhu, S.-Z. Li, An overview of smoothed particle hydrodynamics for simulating multiphase flow, Applied Mathematical Modelling 40 (2016) 9625–9655.
[49] E.W. Washburn, The Dynamics of Capillary Flow, Phys. Rev. 17 (1921) 273–283.
[50] Q. Xu, X. Ma, Z. Cheng, X. Xiao, Z. Ma, Numerical simulation of conduction problem with evaporation based on a SPH model improved by a fractional order convection-diffusion equation, Engineering Analysis with Boundary Elements 155 (2023) 668–681.
[51] G. Yang, D. Chai, Z. Fan, X. Li, Capillary Condensation of Single- and Multicomponent Fluids in Nanopores, Ind. Eng. Chem. Res. 58 (2019) 19302–19315.

[52] Q. Yang, P.Z. Sun, L. Fumagalli, Y.V. Stebunov, S.J. Haigh, Z.W. Zhou, I.V. Grigorieva, F.C. Wang, A.K. Geim, Capillary condensation under atomic-scale confinement, Nature 588 (2020) 250–253.
[53] X. Yang, S.-C. Kong, Smoothed particle hydrodynamics method for evaporating multiphase flows, Phys. Rev. E 96 (2017) 033309.
[54] Y. Yuan, J. Zhang, D. Wang, Y. Xu, B. Bhandari, Molecular dynamics simulation on moisture diffusion process for drying of porous media in nanopores, International Journal of Heat and Mass Transfer 121 (2018) 555–564.
[55] V.V. Zhakhovsky, A.P. Kryukov, V.Yu. Levashov, I.N. Shishkova, S.I. Anisimov, Mass and heat transfer between evaporation and condensation surfaces: Atomistic simulation and solution of Boltzmann kinetic equation, Proceedings of the National Academy of Sciences 116 (2019) 18209–18217.
[56] J. Zhong, J. Riordon, S.H. Zandavi, Y. Xu, A.H. Persad, F. Mostowfi, D. Sinton, Capillary Condensation in 8 nm Deep Channels, J. Phys. Chem. Lett. 9 (2018) 497–503.